

# Effect of initial conditions of modeled PDFs on droplet characteristics for coalescing and evaporating turbulent water spray used in fire suppression applications

Sam S. Yoon<sup>a,\*</sup>, Ho Y. Kim<sup>a</sup>, John C. Hewson<sup>b</sup>

<sup>a</sup>Mechanical Engineering Department, Korea University, Anamdong, 5-Ga, Sungbukgu, Seoul 136-713, Republic of Korea

<sup>b</sup>Fire Science and Technologies, P.O. Box 5800, Albuquerque, NM 87185-1135, USA

Received 12 June 2006; received in revised form 1 November 2006; accepted 4 January 2007

Available online 1 March 2007

## Abstract

Parametric studies were conducted for a coalescing and evaporating turbulent water spray using a stochastic separated flow technique that includes submodels for droplet dynamics, heat and mass transfer, and droplet–droplet binary collisions. While the initial droplet size distribution, in general, is not known due to the difficulty in the optical access to the nozzle exit region, the size distribution is modeled using the analytical PDFs (probability density functions) such as log-normal, Rosin–Rammler, Gaussian, and Nukiyama–Tanasawa distribution model. Standard deviation of the PDFs is varied and their effects on droplet size and speed distribution in the downstream are reported. The arithmetic mean droplet size at the nozzle exit, which is used as input for simulations, was extrapolated using the existing experimental data obtained at downstream locations.

© 2007 Elsevier Ltd. All rights reserved.

**Keywords:** Turbulent spray; Droplet distribution; Initial condition; Rosin–Rammler; Log-normal; Gaussian

## 1. Introduction

Rapid fire suppression is a necessity for modern vehicle crew compartments and for enclosures containing critical equipment susceptible to fire damage. In a case where a fuel tank of a military or civilian vehicle is punctured by arsenal ammunition, liquid fuel is transported as atomized droplets as shown in Fig. 1(a) and, hence, forming a fuel-pool and flammable gas near the tank [1]. The spark from the incendiary in the flammable gas region initiates an ignition event which leads to a sustained pool fire. Another case in point is that of a moving vehicle collisions with flammable storage (i.e., gas station, liquid natural gas facilities, gas/oil pipeline), or a moving fuel-tank crashing against a building (i.e., the 9/11 terrorist attack) as shown in Fig. 1(b) of Ref. [2]. For these applications, high-momentum sprays are useful for quickly dispersing condensed-phase suppressants to the fire and the surrounding compartment to minimize

the thermal insult to its occupants. Because of the high momentum of the water suppressant spray, water atomized droplets are expected to penetrate the flame and reach the fuel surface; hence, surface cooling would occur, which reduces the pyrolysis rate and so the rate of fuel supply to the flame zone. In addition, small water droplets with diameters of the order of tens of microns behave as a mist or cloud, which attenuates the radiant heat of the flame by absorbing and scattering the infrared wavelength characteristics of luminous flame. The high-speed water spray of great momentum, containing small droplets, is considered an ideal fire suppression spray.

The current paper focuses on the predictive modeling of a specific nozzle, typical of those that might be used to provide suppression in a compartment in a matter of seconds or less. Droplet size and velocity measurements are presented to help develop the appropriate initial conditions for this nozzle and to air in evaluating the model.

Understanding the size distribution of a spray at the liquid core region, where liquid becomes atomized, has always been an arcane subject in the atomization

\*Corresponding author. Tel.: +82 2 3290 3376; fax: +82 2 926 9290.  
E-mail address: [skyoona@korea.ac.kr](mailto:skyoona@korea.ac.kr) (S.S. Yoon).

### Nomenclature

$B$	spalding or mass transfer number
$c_p$	specific heat
$C_D$	drag coefficient
$D$	droplet or particle diameter
$D_M$	mass diffusivity
$D_{10}$	arithmetic mean diameter
$D_{32}$	Sauter mean diameter
$f(D)$	probability density function (PDF)
$g$	gravitational acceleration
$h_v$	heat of vaporization
$k$	thermal conductivity
$Le$	Lewis number
$m$	droplet or particle mass
$Oh$	Ohnesorge number
$Pr$	Prandtl number
$q$	Rosin–Rammler dispersion coefficient
$Re$	Reynolds number
$Sc$	Schmidt number
$T$	temperature
$\vec{u}$	velocity

$We$	Weber number
$x$	(or $z$ ) axial axis
$X$	characteristics mean diameter of the Rosin–Rammler PDF
$y$	(or $r$ ) radial axis
$Y$	mass fraction

### Greek letters

$\theta$	cone angle
$\mu$	kinematic viscosity
$\nu$	dynamic viscosity
$\rho$	density
$\sigma$	Gaussian deviation
$\sigma_{ln}^*$	dimensionless log-normal deviation

### Subscripts

$( )_c$	parcel property
$( )_f$	film property
$( )_g$	gas property
$( )_p$	droplet or particle property

community. The recent experiment by MacPhee et al. [3], and the computational work by Yoon [4], have shed light on this subject. (See Fig. 2(a) for the demonstration of the computational capability.) However, the photographic

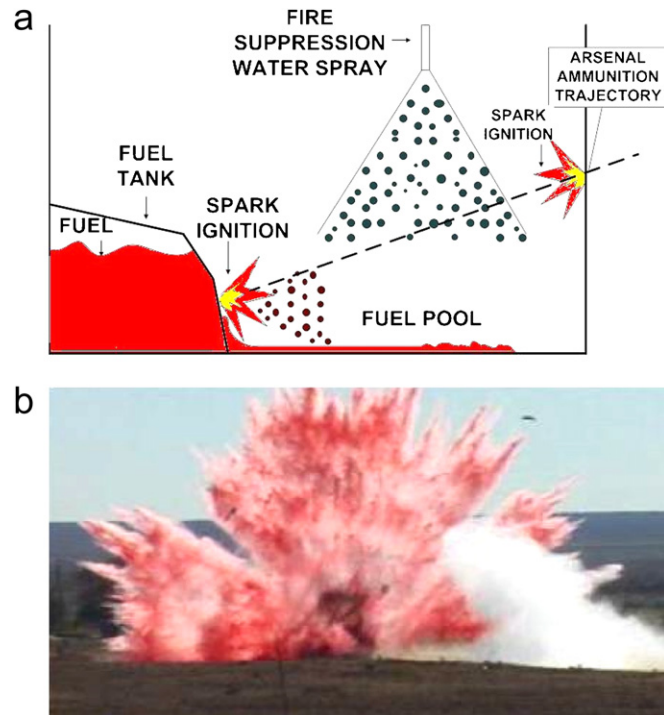


Fig. 1. (a) Live fire event illustrating liquid fuel spray ignition and sustained pool fire. (b) Atomized drop formation due to splashing upon the wall-impact of large scale fuel tank without ignition [2].

assessment by MacPhee et al. [3], which utilized the X-ray technique, has not yet revealed the complex shape of the liquid core, or the distribution shape of atomized droplets. The computational work of Yoon [4] and Park et al. [5], showed what was until now, the unknown shape of the liquid core and the distribution shape of the atomized

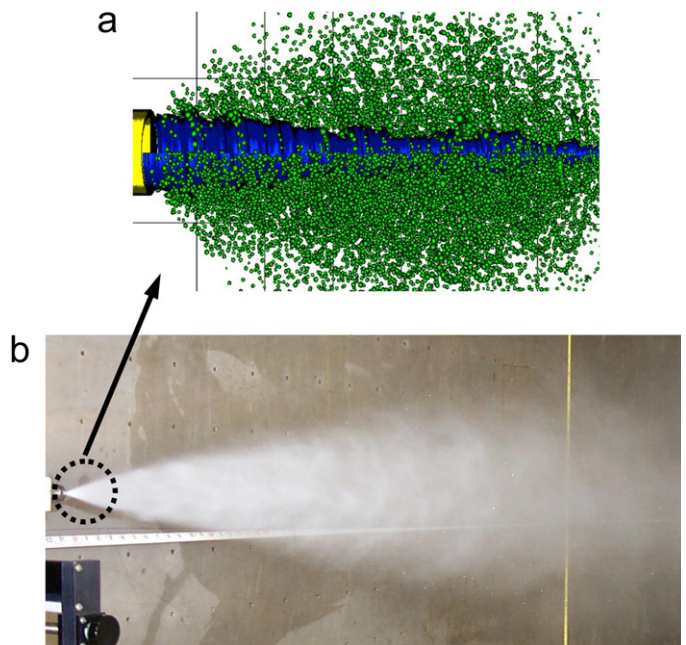


Fig. 2. (a) Near-field view of the high-pressure water spray at the liquid core region [4]. (b) Experimental image of near field view of the evaporating and coalescing turbulent water jet.

droplets. Yoon [4], concluded that the Nukiyama–Tanasawa distribution could be used as a reasonable model for the initial size distribution shape, while Park et al. [5], noted that the Rosin–Rammler distribution shape also could well be used for the initial distribution model. Naturally, a question arises; “Can other distribution models (such as log-normal, Gaussian, and Nukiyama–Tanasawa; see Babinsky and Sojka, [6]), be used as a reasonable model as well?”. We attempt to address this issue by investigating the effect of these modeled PDFs on the droplet characteristics for the high speed turbulent water jet, where droplets are evaporating and coalescing.

It is presumed that the secondary atomization does not occur since the gas-based mean Weber number is found to be below 12 [7] under the given experimental conditions; the turbulence alone acts as a dominant source of instability, as opposed to the instability driven by the shear-layer between the injected liquid and air. Here we assume an instantaneous atomization event, which yields the distribution of droplets, modeled by the presumed PDFs of Rosin–Rammler, log-normal, Gaussian, and Nukiyama–Tanasawa, at the nozzle exit.

The arithmetic mean droplet size at the liquid core, whose value was around 40  $\mu\text{m}$ , was extrapolated using the experimental data obtained at downstream locations. All PDFs satisfied the mean value of 40  $\mu\text{m}$  while their shapes were dependent on the value of the standard deviation, i.e., the dimensionless dispersion coefficient ( $q$ ) of the Rosin–Rammler varied from 1.5 to 4.5; the dimensionless deviation ( $\sigma_{\ln}^*$ ) of the logarithm of the diameter varied from 0.2 to 0.8; the dimensional deviation ( $\sigma$ ) of the Gaussian distribution varied from 0.25 $D_{10}$  to 1.00 $D_{10}$  (where  $D_{10}$  is the arithmetic mean diameter), and the governing parameter of the Nukiyama–Tanasawa distribution ( $p$ ) varied from 1 to 8. The effects of these parametric variations of the PDFs on the droplet characteristics are reported.

To reduce the computational cost, a stochastic Lagrangian particle tracking method was adopted for these parametric studies [8]. The stochastic model includes the particle–parcel submodel in which one parcel represents many particles, for the purpose of reducing the computational cost [9]. To properly account for the particle–parcel coupling effect, the parcel distribution shape of  $\chi^2$ -type was used [10]. The reference by Hewson and Yoon [11] is suggested for further details. Experimental data are also presented to show the droplet segregation phenomenon which occurs in both axial and radial directions. The joint PDFs [12], of the experimental droplet size and velocity at various physical locations are also reported in conjunction with the droplet segregation phenomenon.

## 2. Computational model

Simulations are conducted using the Vulcan fire simulation code, which has been extended to handle the dilute

multiphase flow physics found in evaporating and reacting sprays [8]. The spray model is coupled with the Navier–Stokes solver, which is based on a Reynolds averaged Navier Stokes (RANS) formulation, employing a standard  $k$ – $\epsilon$  turbulence closure model [13]. The gas-phase flow is calculated on an Eulerian staggered Cartesian grid, using the SIMPLEC method [14].

The condensed phase evolves using a Lagrangian approach, based on the stochastic separated flow model [15,16]. Evolution equations for collections of droplets with similar sizes and initial conditions (denoted as parcels), are used to reduce computational cost. A sufficient number of parcels are used to ensure an adequate resolution of the spray physics and the measured droplet statistics. Statistical variations in droplet size and velocity are imposed as initial conditions to simulate the liquid jet breakup process, which phenomenon was experimentally shown by Sallam et al. [17,18]. The parcels are advanced under the influence of modeled turbulent fluctuations in the gas-phase properties.

### 2.1. Conservation of mass

The correlation by Ranz and Marshall [19,20] is used for the evaporation model,

$$\frac{dm}{dt} = \pi D \frac{\mu_f}{Sc_f} \left[ 2 + \frac{2}{3} Re^{1/2} Sc_f^{1/3} \right] \ln(1 + B_m), \quad (1)$$

where  $m$  is the droplet mass,  $D$  is the droplet diameter,  $Sc_f = \nu_f/D_M$  is the film Schmidt number,  $D_M$  is the mass diffusivity,  $Re = \rho_g D |\vec{u}_p - \vec{u}_g|/\mu_g$  is the droplet Reynolds number, and  $B_m = (Y_f - Y_g)/(1 - Y_f)$  is the Spalding or mass transfer number that characterizes the concentration gradients at the film interface. In these and all subsequent expressions, the subscripts ( $\cdot$ )<sub>g</sub> represent gas properties, ( $\cdot$ )<sub>p</sub> represent droplet/particle properties, and ( $\cdot$ )<sub>f</sub> represent droplet film properties for the thin-film approximation of the liquid–gas interface at the droplet surface.

### 2.2. Conservation of momentum

The momentum equation for a small rigid sphere in a non-uniform flow is derived by Maxey and Riley [21]. As discussed by Faeth [16], if the ratio of particle to gas densities is large (i.e.  $\rho_p/\rho_g \gg 1.0$ ) then the predominant forces generally consist of the drag and body forces leading to a relatively simple form of the momentum equation,

$$m \frac{d\vec{u}_p}{dt} = \frac{\pi}{8} \rho_g D^2 C_D |\vec{u}_g - \vec{u}_p| (\vec{u}_g - \vec{u}_p) + m\vec{g}, \quad (2)$$

where  $\vec{u}_p$  is the droplet velocity and  $\vec{u}_g$  is the gas phase velocity around that particle and  $\rho_g$  is the gas phase density. The last term on the right-hand side is the body force term due to gravity. The coefficient of drag,  $C_D$ , is modeled using the standard drag coefficient relations for a sphere in a uniform flow [16,21].

### 2.3. Conservation of energy

The droplet temperature evolution is a balance between convection and evaporation. The droplet thermal energy can then be expressed as

$$mc_{v,d} \frac{dT}{dt} = \dot{Q}_c + \dot{Q}_e, \quad (3)$$

where

$$\dot{Q}_c = \pi d \frac{\mu_f}{Pr_f} c_{p,f} (T_g - T) \left[ 2 + \frac{k}{F(B_t)} Re^{1/2} Pr_f^{1/3} \right] \frac{\ln(1 + B_t)}{B_t},$$

$$\dot{Q}_e = mh_{v,f}.$$

In these expressions,  $Pr_f = \nu_f / \alpha_f = c_{p,f} \mu_f / k_f$  is the film Prandtl number and  $h_{v,f}$  is the heat of vaporization. A “thin-skin” model is used and conditions at the droplet surface are obtained iteratively by equating heat flux to the droplet with droplet heating and enthalpy associated with vaporization [16]. The relationship between the quasi-steady state film temperature and the fluxes to the droplet are modeled by the Spalding heat transfer number,  $B_t = [1 + B_m]^{Le_f} - 1$ .

### 2.4. Collision, breakup, and turbulence models

Droplet–droplet collisions occur during the atomization of a liquid jet. For some applications, accounting for these collisions may be important in reproducing observed mean drop sizes downstream of primary atomization. Collisions of pairs of computational parcels are treated using a statistical process description. The procedure starts by checking to see if two parcels occupy the same computational cell. If they do not share the same cell then it is assumed that collisions cannot occur. If they do share the same cell then the parcel containing the larger drops are designated as the collectors and parcel containing the smaller drops designated as the donors. The expected frequency of collisions between by one collector with all the droplets is assumed to obey the collision-criteria suggested by Ko et al. [22]. This approach only accounts for either droplet–droplet “bouncing” or “coalescence”, and not droplet–droplet “shattering” effect that produces additional drops. The “shattering” effect may become important for the head-to-head colliding sprays [23]. Since all droplets are moving in the same direction in our spray, the “shattering” is highly unlikely to occur. The Taylor analogy breakup (TAB) model of O’Rourke and Amsden [24] is adopted to indicate the significance of droplet breakup in this study. The model assumes a direct analogy between the oscillation of a droplet and a forced spray-mass-damper system [24].

Turbulence models are introduced at the parcel and sub-parcel level to account for the effect of local fluctuations in the velocity field while the rest of the thermo-physical variables are approximated by their corresponding time averaged values. The velocity–fluctuation models serve to increase the droplet dispersion, mimicking the effects of

unresolved turbulent eddies. These unresolved turbulent motions are significant for the present high-pressure spray that generates substantial turbulent kinetic energy. These unresolved turbulent motions are decomposed into parcel and sub-parcel models.

The parcel turbulence model accounts for the effects of turbulent eddies perturbing the parcel trajectory and is based on the random walk model of Gosman and Ioannides [25], as modified by Shuen et al. [26]. This model essentially perturbs the gas velocity  $\vec{u}_g$  in Eq. (2) by an amount randomly selected from a Gaussian distribution over the velocity scales expected based on the turbulent kinetic energy. Within a parcel, the spatial distribution of particles is assumed to be of Gaussian form. The standard deviation of this spatial distribution evolves with time for each parcel at a velocity,  $\vec{u}_p$ , with the evolution equation for  $\vec{u}_p$  being essentially Eq. (2) except that the velocities are replaced by  $\vec{u}_p$  and the fluctuating gas velocity in the manner of Zhou and Yao [27]; the buoyant term is also neglected in particle dispersion since it acts equally on all particles.

### 2.5. Initial conditions

In the description of a spray or particulate flow, it is generally necessary to define the size distribution of the particles as an initial condition. Typically the distribution of particles corresponds to one of the standard distribution functions. Typical distribution functions include the Rosin–Rammler distribution, the normal or Gaussian distribution and the log-normal distribution. These and other distributions are reviewed by Babinsky and Sojka [6].

In computational descriptions of the particulate flow, it is usually impossible to track all of the individual particles; thus alternative approaches are typically employed. One approach is to track parcels [8]. For conservation equations describing these parcels to accurately represent the evolution of all particles, the particles in a parcel generally are restricted to a fixed diameter. If the number of particles in each parcel is identical, then the size distribution of parcel should follow the size distribution of particles. However, it is computationally more expedient to force the mass of each parcel to be identical. Thus, the number of particles per parcel is inversely proportional to the particle mass. Equivalently, the number of particles per parcel is proportional to  $D^{-3}$  where  $D$  is the diameter of the particle. In this case, the parcel distribution,  $f_c(D)$ , differs from the particle distribution,  $f_p(D)$ .

$$f_c(D) = AD^3 f_p(D), \quad (4)$$

where  $A$  is a scaling factor so that  $f_c(D)$  can be properly normalized. O’Rourke [10] provides the corresponding parcel distribution for the given chi-square ( $\chi^2$ ) distribution while Hewson and Yoon [11] provides the corresponding parcel distributions for the Rosin–Rammler, log-normal, and Gaussian distributions. These PDFs are summarized in Table 1 and the corresponding expressions for size distributions of particle and parcel are listed in Table 2.

Table 1  
The PDFs for particle and parcel for the Rosin–Rammler, log-normal, Gaussian, and Nukiyama–Tanasawa distributions

	Particle PDF, $f_p$	Parcel PDF, $f_c$
Rosin–Rammler	$f_{p,rr}(D) = q \frac{D^{q-1}}{X^q} \exp\left[-\left(\frac{D}{X}\right)^q\right]$ where $q$ is the dispersion coefficient  $X = D_{10}/\Gamma(1/q + 1)$ where $\Gamma$ is the complete Gamma function	$f_{c,rr}(D) = A_{rr} D^3 f_{p,rr}(D)$ $A_{rr} = \frac{1}{X^3 \Gamma(\frac{3}{q} + 1)}$
Log-normal	$f_{p,ln}(D) = \frac{1}{\sqrt{2\pi}\sigma_{ln}^* D} \exp\left[-\left(\frac{\ln D - \ln D_{ln}}{2\sigma_{ln}^{*2}}\right)^2\right]$ where $D_{ln} = \exp(\ln D) = D_{10}/\exp(0.5\sigma_{ln}^{*2})$ $\sigma_{ln}^*$ is the dimensionless standard deviation of the logarithm of the diameter	$f_{c,ln}(D) = A_{ln} D^3 f_{p,ln}(D)$ $A_{ln} = 1/\exp[3\bar{x} + (9/2)\sigma_{ln}^{*2}] = \frac{1}{D_{ln}^3 \exp(9\sigma_{ln}^{*2}/2)}$ where $\bar{x} = \ln D_{ln}$
Gaussian	$f_{p,g}(D) = \frac{1}{\sqrt{2\pi}\sigma} \exp\left[-\frac{(D-\bar{D})^2}{2\sigma^2}\right]$ where $\sigma$ is the dimensional standard deviation of the diameter  $\bar{D}$ is the mean diameter	$f_{c,g}(D) = A_g D^3 f_{p,g}(D)$ $A_g \bar{D}^3 = A_g^* = \frac{\sqrt{2\pi}}{(2\sigma^{*3} + \sigma^*)a' + \sqrt{\pi/2}(3\sigma^{*2} + 1)(1+c')}$ $a' = \exp(-0.5/\sigma^{*2})$ $c' = \text{erf}\left(\frac{1}{\sqrt{2}\sigma^*}\right)$ , note $\text{erf}$ is the error function $\sigma^* = \sigma/\bar{D}$ where $( )^*$ is the dimensionless quantity
Nukiyama–Tanasawa	$f_{p,nt}(D) = a_{nt} D^p \exp[-bD^c]$ where $a_{nt} = \frac{cb^{(p+1)/c}}{\Gamma[\frac{p+1}{c}]}$ is the normalizing factor  The coefficients, $b$ , $c$ , and $p$ are the dimensional parameters	$f_{c,nt}(D) = A_{nt} D^3 f_{p,nt}(D)$ $A_{nt} = \frac{cb^{(p+4)/c}}{a_{nt} \Gamma[\frac{p+4}{c}]}$

Table 2  
The size distributions for particle and parcel for the Rosin–Rammler, log-normal, Gaussian, and Nukiyama–Tanasawa distributions

	Particle size	Parcel size
Rosin–Rammler	$D = X \left(\ln\left[\frac{1}{1-RN}\right]\right)^{1/q}$ $RN$ is the random number ranging from 0 to 1	$D = X \left(P^{-1}\left[\frac{3}{q} + 1, RN\right]\right)^{1/q}$ where $P^{-1}$ is the inverse of the incomplete gamma function (see Ref. [28])
Log-normal	$D = D_{ln} \exp[\sqrt{2}\sigma_{ln}^* \text{erf}^{-1}(2RN - 1)]$	$D = D_{ln} \exp[\sqrt{2}\sigma_{ln}^* \text{erf}^{-1}(2RN - 1) + 3\sigma_{ln}^{*2}]$
Gaussian	$D = \bar{D} + \sqrt{2}\sigma \text{erf}(2RN - 1)$	$RN = \frac{A_g^*}{\sqrt{2\pi}} \left\langle \sigma^* \{a'(1 + 2\sigma^2) - b'[(D^* - 1)^2 + 2\sigma^{*2}]\} \right.$ $\quad \left. + \frac{3\sigma^*}{2} \{(2 - 2D^*)b' - 2a' + \sqrt{2\pi}\sigma^*(c' + d')\} \right.$ $\quad \left. + 3\sigma^* \{a' - b'\} + \sqrt{\frac{\pi}{2}} \{c' + d'\} \right\rangle$ $b' = \exp\left(-\frac{(D^*-1)^2}{2\sigma^{*2}}\right)$ $d' = \text{erf}\left(\frac{D^*-1}{\sqrt{2}\sigma^*}\right)$ Note: This expression is implicit that it needs to be solved iteratively. Explicit expression for the parcel size of the Gaussian distribution cannot be obtained.
Nukiyama–Tanasawa	$D = \left\{\frac{1}{b} P^{-1}\left[\frac{p+1}{c}, 1 - RN\right]\right\}^{1/c}$	$D = \left\{\frac{1}{b} P^{-1}\left[\frac{p+4}{c}, 1 - RN\right]\right\}^{1/c}$

3. Experimental apparatus

The water spray used for the purpose of model evaluation is produced using a converging nozzle manufactured by *Spraying Systems Co.*, Wheaton, IL.

The internal converging angle is approximately 40°, and is followed by a constant-diameter section of length 3.31 mm. The water spray is directed horizontally with a liquid core speed of  $U = 80$  m/s, a diameter of  $d = 2$  mm, a mass flow rate of  $\dot{m} = 0.25$  kg/s, and a liquid and gas

temperature of  $T = 300$  K. The dimensionless parameters are  $Re = Ud/\nu = 142\,857$ ,  $We = \rho U^2 d/\sigma = 174\,387$ ,  $We_g = \rho_g U^2 d/\sigma = 215$ , and  $Oh = \mu/\sqrt{\rho d \sigma} = 0.0023$ . Since  $We_g > 40$ , the spray is in the atomization regime [29]. The experimental image of the spray is shown in Fig. 2(b).

Radial profiles of particle sizes and axial velocities were measured with a phase Doppler particle analyzer (PDPA). Measurements were conducted at four axial locations, beginning at  $x = 48$  mm and continuing to  $x = 250$ , 480, and 810 mm downstream of the spray nozzle. These distances correspond to 24, 125, 240 and 405 in

terms of distances normalized by the nominal nozzle diameter,  $d = 2$  mm. Results are presented in terms of quantities averaged at a given downstream distance and radial location. At each location, data were collected for a fixed time, 5 s, in an attempt to determine the number density of particles at that location. We report results for radial locations where approximately 10 000 particles per second were counted; statistics at other locations are insufficient for reporting results. Uncertainties for the averaged particle diameters and velocities are estimated to be 10–15% in accordance with our experience [30]; these uncertainties are likely dominated by systematic errors.

Table 3  
Experimental data collected at various axial locations

$x$ (mm)	0	48	250	480	810
$\Delta y$ (mm)	1	20	90	125	170
$D_{10}$ ( $\mu\text{m}$ )	40.63	46.85	72.39	79.66	71.60
$D_{32}$ ( $\mu\text{m}$ )	75.78	83.49	90.77	117.71	119.41
$D_{32}/D_{10}$	1.865	1.782	1.254	1.478	1.668
$q$	1.496	1.576	2.910	2.050	1.712

Nozzle diameter is  $d = 2$  mm. At nozzle exit ( $x = 0$  mm), both  $D_{10}$  and  $D_{32}$  are extrapolated.

#### 4. Parametric studies

All simulations run for a duration of 2 s on a  $1.2\text{ m} \times 0.8\text{ m} \times 0.8\text{ m}$  domain. A  $52 \times 43 \times 43$  Cartesian grid is employed. The flow is essentially steady after 0.2 s and statistics are collected from 0.2 to 2.0 s at intervals of 0.0002 s. Parcels are injected at a rate of 133 333 per second; the mass associated with each parcel is approximately  $1.875 \times 10^{-6}$  kg of water. The number of droplets per parcel depends upon the droplet diameter, as deter-

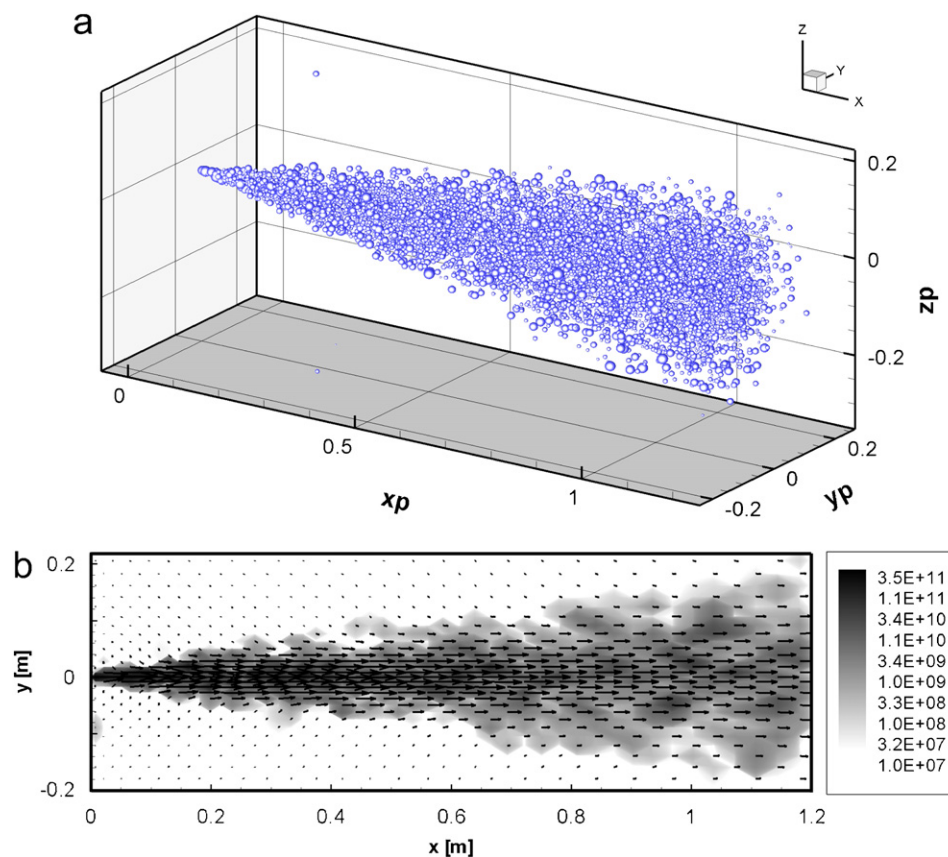


Fig. 3. (a) Instantaneous snapshot of spray calculation at quasi-steady state. (b) Gas velocity vectors in the  $z = 0$  plane, indicating centrally directed entrainment. Superimposed contours indicate the local particle number density.

mined in the previous section, and sufficient to account for the initial mass associated with the parcel.

Here, it is noteworthy that the spray of the current study is a “coalescence” dominating spray. The collision between the binary droplets is expected to occur at the liquid core region as the region is highly populated with atomized droplets. As for the modeling, the collision event is recorded when two colliding droplets share the same cell and the collision frequency between the binary droplets is higher than the critical value [22,24].

As mentioned earlier, the averaged droplet size at the nozzle exit was extrapolated using the experimental data at downstream locations (see Table 3). A simple quadratic least square fit was used for the extrapolation. In Table 3, the experimental data collected at various axial locations are summarized. Under the cone-angle (approximately  $\theta \cong 15^\circ$ ), the width of the jet increases as the axial location increases. Both  $D_{10}$  and  $D_{32}$  also grow when the axial location is increased, because of the gradual disappearance of the smaller droplets further downstream. Smaller

droplets have a tendency to evaporate quickly, and coalescence also causes a shift to larger droplet sizes downstream. The rate at which  $D_{32}$  grows from  $x = 48$  to 480 mm is greater than that of  $D_{10}$ . This pattern indicates the existence of relatively larger droplets dominating at a downstream location, as  $D_{32}$  is greatly affected by the larger droplets (i.e.,  $D_{32} \propto D^3/D^2$ ). Evaporation plays a role in reducing  $D_{10}$  at  $x = 810$  mm as surrounding air causes droplets to evaporate quickly further downstream. Using the downstream data of Table 3, the droplet data at the nozzle exit (i.e.,  $x = 0$ ) are extrapolated. The extrapolated arithmetic mean droplet size,  $D_{10} = 40.63 \mu\text{m}$ , is used for all spray simulations herein.

In Fig. 3(a), a snapshot of the spray at the quasi-steady state is shown. As indicated, larger droplets have a tendency to locate at the larger radial location, whereas smaller droplets tend to conglomerate toward the center of the spray. This droplet segregation (or gradation) is caused by the entrainment phenomenon whose effect is eminent over the smaller droplets, while its effect is nearly absent

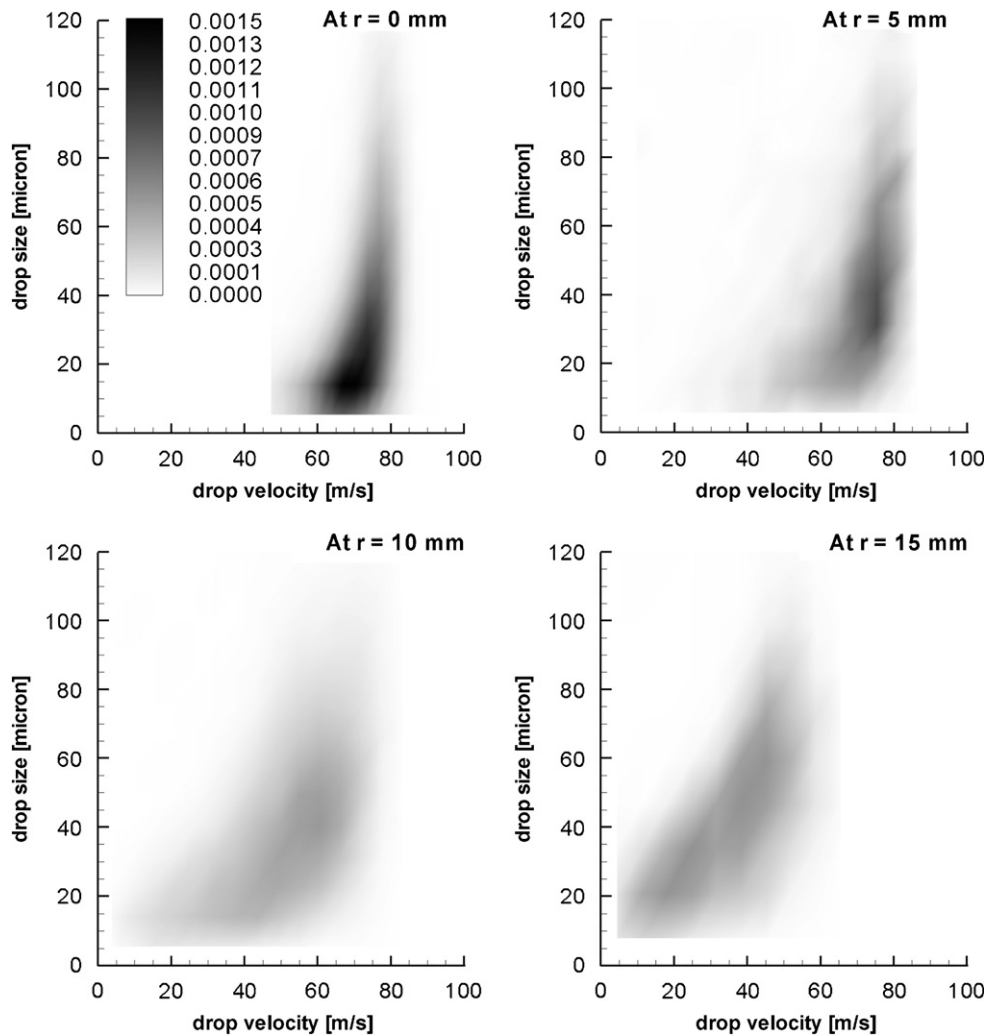


Fig. 4. Joint probability density function (JPDF) distributions based on the experimental data obtained at  $z = 48$  mm at various radial locations.

for the relatively larger droplets, which carry larger momentum. Fig. 3(b) shows the entrainment phenomenon, which starts to occur at the nozzle exit ( $x = 0$ ). The contour level is scaled with the droplet number density. In Fig. 3(b), it is observed that the high concentration of the number density lies toward the spray's center. This, so-called "droplet gradation," is manifested in the experiment as well. As shown in the joint PDF (size and speed) of the experimental data in Fig. 4, the smaller, faster droplets reside at the center (see  $y = 0$  mm plot) while the larger, slower droplets (due to drag), reside at the larger radial locations. Observe the trend of the plots from  $y = 0$  to 15 mm in Fig. 4. Thus, the droplet gradation phenomenon is consistently observed both in this simulation and in the experiment. It is worthwhile to note that the axial location of the data presented in Fig. 4, is at  $x = 48$  mm, which is around 24 nozzle diameter downstream. Thus, the droplet gradation may be said to occur quite quickly—as soon as

droplets are formed subsequent to the atomization at the liquid core region. Fig. 5 shows the JPDF variation in the axial direction ranging from  $x = 48$  to 810 mm. It is noted that the plot representing the JPDF at  $x = 48$  mm is the averaged distribution of all radial locations of Fig. 4, i.e.,  $y = 0, 5, 10,$  and  $15$  mm. Thus, the similarity between the JPDF at  $x = 0$  mm in Fig. 4 and the JPDF at  $x = 48$  mm in Fig. 5 can be observed. As shown in Fig. 5, the relatively higher probability of larger droplets at the downstream location than smaller droplets upstream is indicative of the disappearance of the smaller droplets due to evaporation and coalescence. The trend of droplet velocity shows that drag decreases velocity as droplets travel downstream.

Fig. 6 shows the various PDFs of the Rosin–Rammler distribution function for  $q = 1.5, 2.5, 3.5,$  and  $4.5$ . The relevant input data are shown in Table 4. Here, the arithmetic mean diameter,  $D_{10}$ , at the nozzle exit is

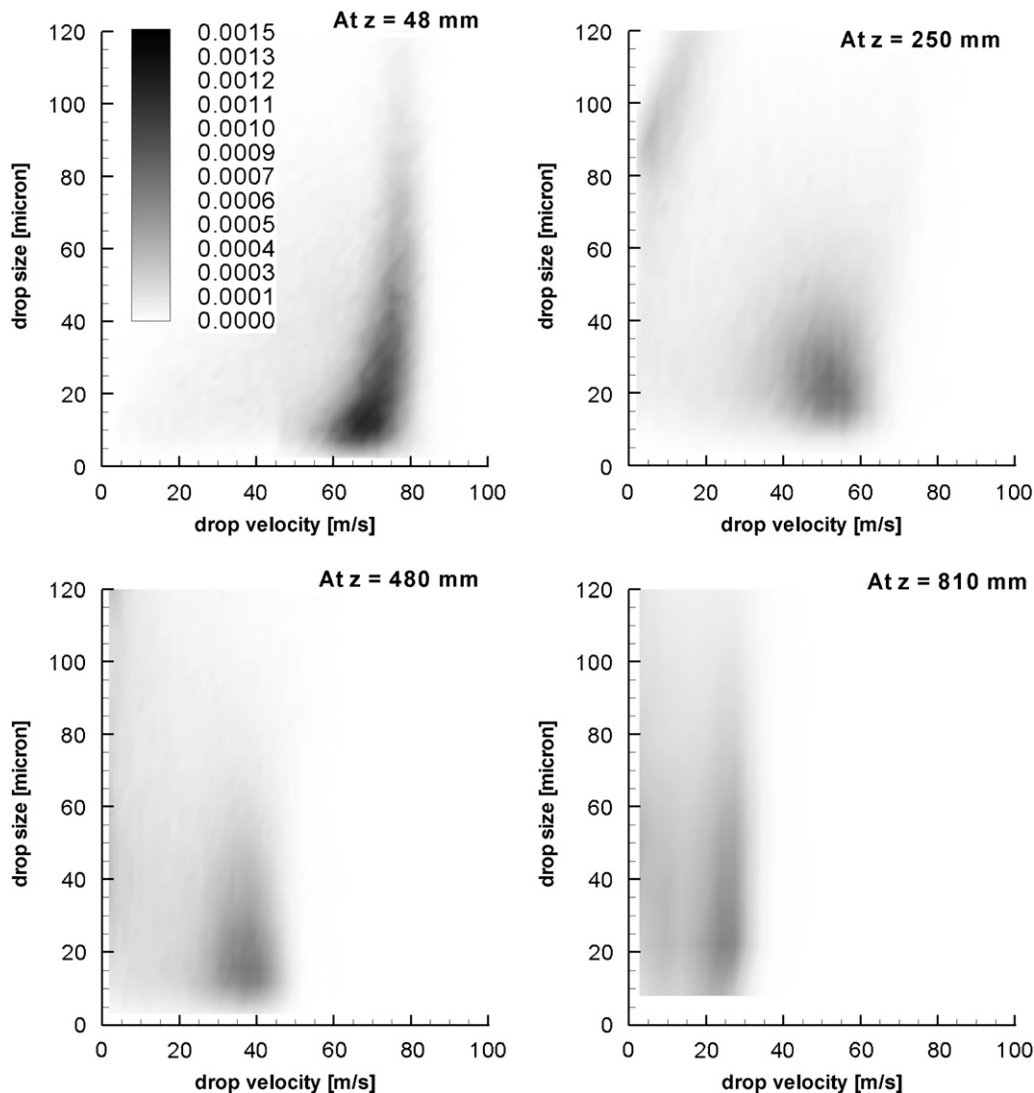


Fig. 5. Joint probability density function (JPDF) distributions based on the experimental data obtained at various axial locations.

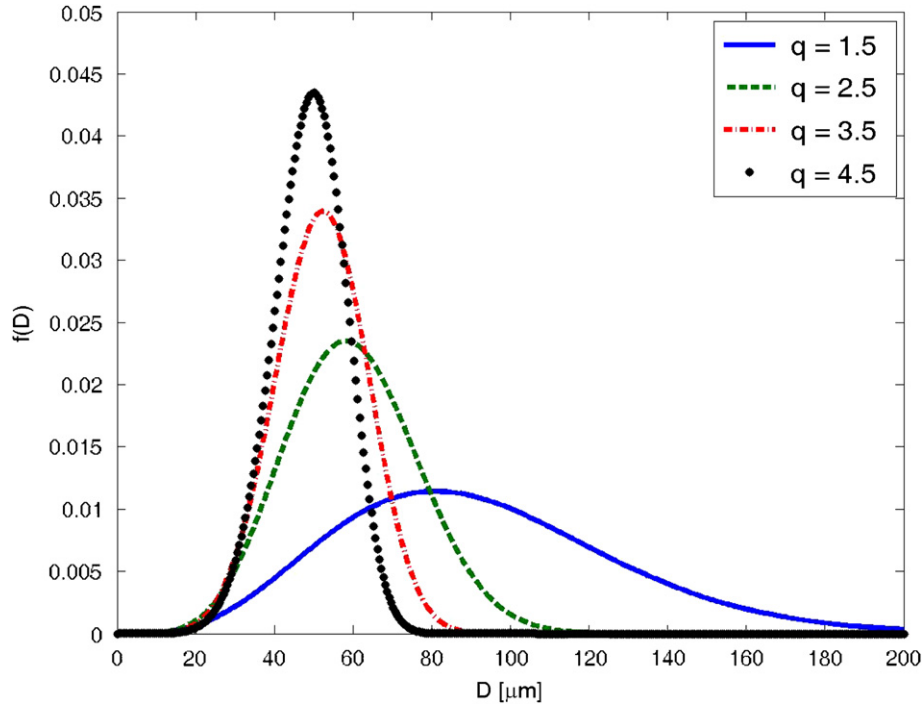


Fig. 6. Analytical PDFs of the Rosin–Rammler distribution for the various dispersion coefficient,  $q$ .

Table 4  
Input parameters for the initial conditions using Rosin–Rammler PDF

Case	$q$	$\Gamma(1/q + 1)$	$X$ ( $\mu\text{m}$ )
1	1.5	0.9027	45.01
2	2.5	0.8873	45.79
3	3.5	0.8997	45.16
4	4.5	0.9126	44.52

Note: The mean diameter,  $D_{10} = X\Gamma(1/q + 1) = 40.63 \mu\text{m}$ , remained constant.

fixed as  $D_{10} = 40.63 \mu\text{m}$  while the characteristic mean diameter of the Rosin–Rammler PDF,  $X$ , is slightly varied to keep  $D_{10}$  constant under the applied dispersion coefficient,  $q$ .

It is observed that higher  $q$  provides narrower distribution, and vice versa. In Fig. 7, the lowest  $q = 1.5$  gives the best results when compared with the experimental data. The increase in the deviation of the computational results from the experimental data at  $x = 480 \text{ mm}$  downstream location is prominent when applying higher  $q$  values. Higher  $q$  value does not induce as many coalescence events because it produces relatively smaller droplets; the probability for the coalescence event becomes low. At further downstream location  $x = 810 \text{ mm}$ , the effect of the generation of the smaller droplets is, again, prominent as the data indicate the larger deviation (or error) from the experimental results for higher  $q = 2.5, 3.5,$  and  $4.5$ . Only

the lowest  $q = 1.5$  value is able to reproduce the results comparable to the experimental data.

From Figs. 7 and 8, the long time evolution of the spray can be observed. There is a clear segregation of the smaller particles in the inner region of the spray, while larger particles are able to move to the outer regions of the spray. Thus the reduction in the number of smaller particles closer to the centerline of Fig. 3(b) continues throughout the majority of the spray evolution. However, at the farthest downstream distance measured, the distribution of droplets becomes substantially more uniform with radial location,  $y$ . The segregation of small droplets near the centerline can be attributed to the competition between turbulent dispersion and entrainment of air by the spray. Droplets that are dispersed by turbulent fluctuations will move outwards from the center, but their outward motion will be countered by the air entrainment. Air entrainment causes a radially inward velocity in conjunction with the spatial acceleration of the jet. Small particles—those with smaller particle Stokes number—will better follow the mean gas motion which drives them to the spray centerline. Larger particles are less affected by the air entrainment and will follow more ballistic trajectories subject to initial velocity vectors arising from the jet breakup process and turbulent dispersion.

Further downstream, the inward entrainment velocities are reduced to the point where smaller particles are substantially dispersed from the centerline. This is shown  $x = 810 \text{ mm}$  downstream in Fig. 7 where the mean droplet diameter becomes more uniform. The simulations capture

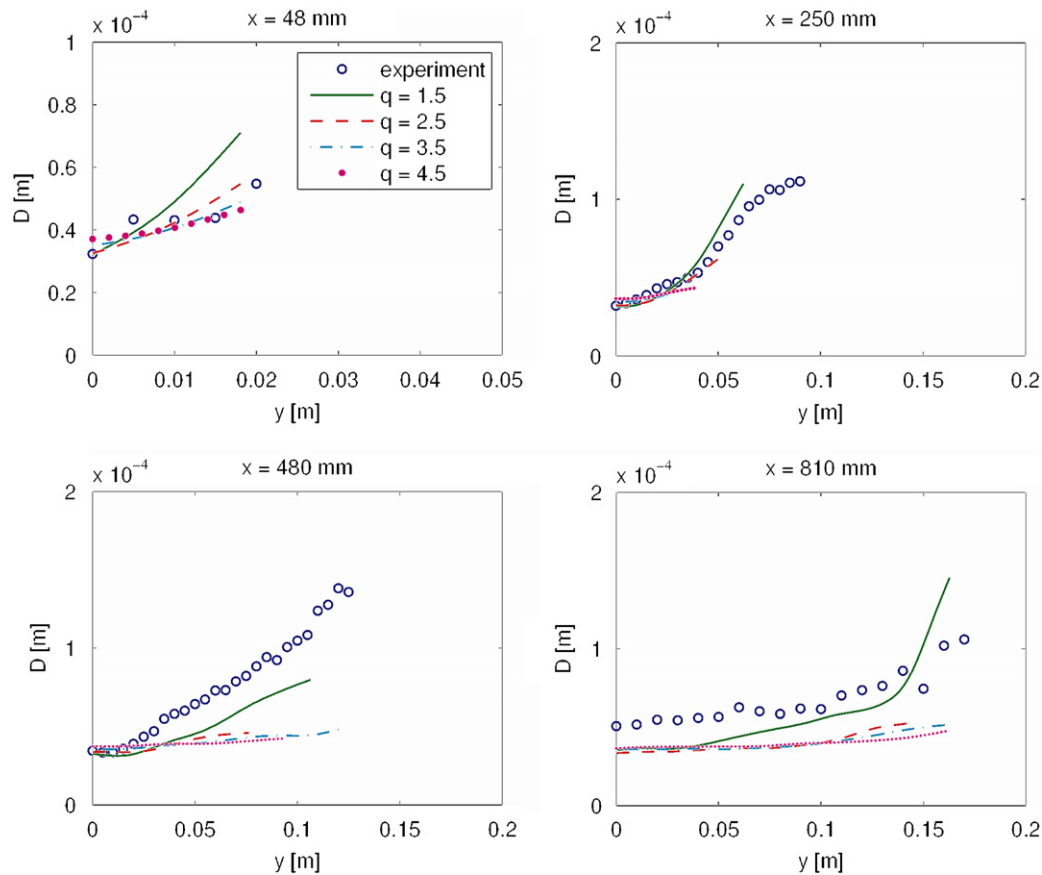


Fig. 7. Mean droplet size variation at different axial locations. The Rosin–Rammler distribution is used for the initial droplet size.

the relative dispersion of the larger and smaller particles with good fidelity, both in the early development where the segregation process is strong, and later when more uniform dispersion is predominant. Also presented in Fig. 8, are the measured axial droplet velocities; these show the reduction in particle velocity associated with spreading of the spray and transfer of momentum to the gas through drag forces. Water spray transfers momentum to the surrounding air and induces a flow (determined from the computational results), with Reynolds numbers on the order of  $10^5$ . Air near the spray centerline is accelerated substantially more than air near the spray edge, so that the outer droplets are slower and experience greater continuous drag. The measurements are compared with simulated droplet velocities in Fig. 8. While the general agreement is good for all cases, there are certain characteristics of the predicted velocity profiles for  $q = 1.5$  case. Computational results tend to over-predict the droplet velocity because of the nature of the stochastic separated flow (SSF) model. The “tailing” behavior of the droplet velocity (shown in Fig. 8 at  $x = 250, 480,$  and  $810$  mm), is attributed to the greater momentum of the large droplets coalesced upstream.

The various PDFs of the log-normal distribution function for  $\sigma_{\ln}^* = 0.2, 0.4, 0.6,$  and  $0.8$  were also used as

an initial condition. The relevant input data are shown in Table 5. Here, the log-normal diameter,  $D_{\ln}$ , is slightly varied to set  $D_{10}$  constant for the varying logarithmic deviation value,  $\sigma_{\ln}^*$ . The results obtained using  $\sigma_{\ln}^* = 0.4$  are under-predicted, while results using  $\sigma_{\ln}^* = 0.6$  are over-predicted. It is likely that there is an optimum value somewhere between  $\sigma_{\ln}^* = 0.4$  and  $0.6$ , which would provide the best initial condition. The tailing behavior of the velocity, previously seen at  $x = 480$  and  $810$  mm in Fig. 8, is also observed, of which effect is predominant for the larger values such as  $\sigma_{\ln}^* = 0.6$  and  $0.8$ .

The various PDFs of the Gaussian distribution function for  $\sigma = 0.25D_{10}, 0.50D_{10}, 0.75D_{10},$  and  $1.00D_{10}$ , where  $D_{10} = 40.63 \mu\text{m}$ , were also used as an initial condition. The relevant input data are shown in Table 6. The results using  $\sigma = 0.75D_{10}$  compares best with the experimental data. Results using the two lower values,  $\sigma = 0.25D_{10}$  and  $0.50D_{10}$ , do not compare well against the experimental data, as their PDF widths are too narrow toward the smaller size distribution; the coalescence events are not properly taken into account.

The PDFs of the Nukiyama–Tanasawa distribution function are shown in Fig. 9 for various values of  $p$  and  $b$ . It should be noted that  $p$  and  $b$  are adjusted so that the arithmetic mean diameter remains constant, as

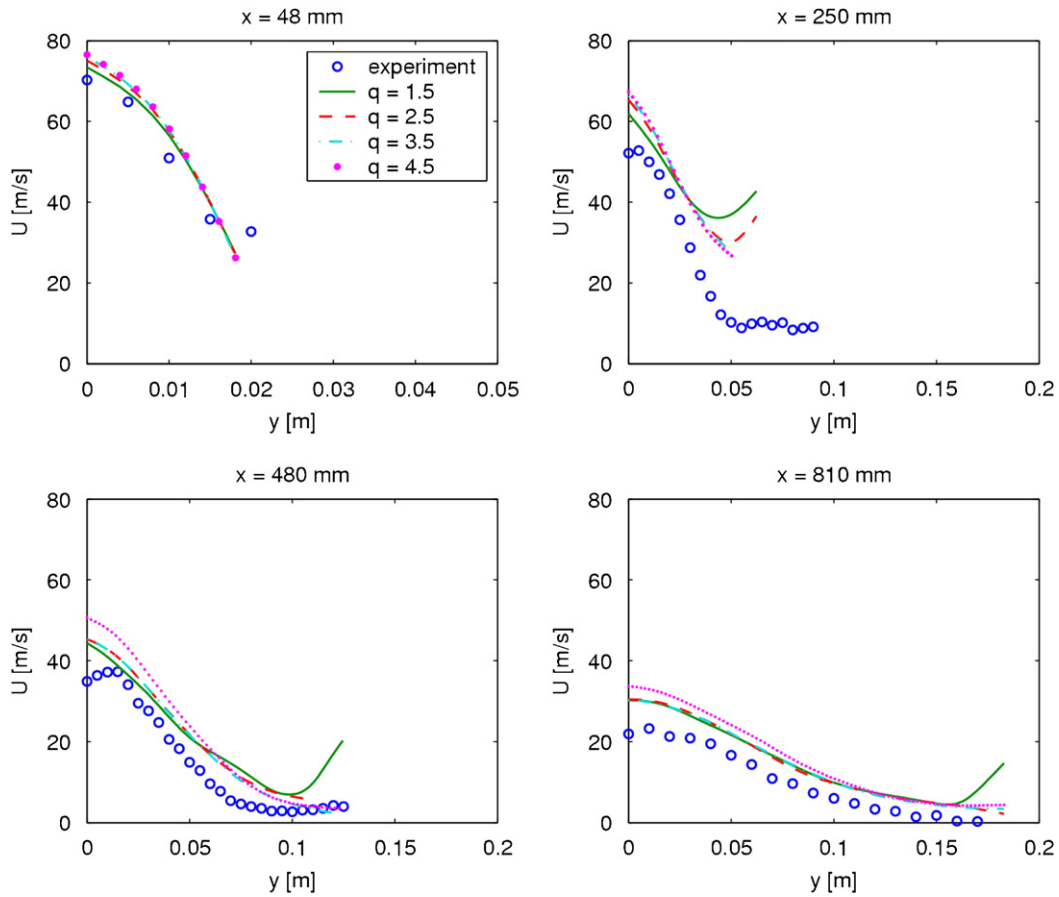


Fig. 8. Mean droplet speed variation at different axial locations. The Rosin–Rammler distribution is used for the initial droplet size.

Table 5  
Input parameters for the initial conditions using log-normal PDF

Case	$\sigma_{in}^*$	$D_{in}$ ( $\mu\text{m}$ )
5	0.2	39.208
6	0.4	36.925
7	0.6	33.411
8	0.8	29.046

Note:  $D_{in} = D_{10} / \exp[\sigma_{in}^{*2}/2]$ , where  $D_{10} = 40.63 \mu\text{m}$  is used.

Table 6  
Input parameters for the initial conditions using Gaussian PDF

Case	$\sigma$
9	$0.25D_{10}$
10	$0.50D_{10}$
11	$0.75D_{10}$
12	$1.00D_{10}$

$D_{10} = 40.63 \mu\text{m}$ . Relevant input data are shown in Table 7. The result using  $p = 1$  over-predicts the droplet size distribution at downstream locations. This over-prediction in the initial droplet size also induces the overly frequent coalescence event and, thus, the computational results do not compare well with the experimental data, as indicated in Fig. 10. On the other hand, the result obtained using  $p = 8$  (which produces relatively smaller droplet size distribution), under-predicts the coalescence event, and thus the overall size distribution is inordinately small. While observing the size comparison for the location at  $x = 250$  and  $810$  mm in Fig. 10, it is clear that  $p = 4$  gives

the best prediction; the similar observation was made for the droplet velocity comparison in Fig. 11. In addition, it seems that the initial condition modeled by the Nukiyama–Tanasawa PDF distribution using  $p = 4$  produces the best result when compared with the results obtained using  $q = 1.5$  of the Rosin–Rammler,  $\sigma_{in}^* = 0.5$  of the log-normal, and  $\sigma = 0.75D_{10}$  of the Gaussian distributions. This conclusion suggests that the Nukiyama–Tanasawa distribution best describes the initial condition, since the distribution has more adjustable parameters, i.e.,  $p$ ,  $b$ , and  $c$  (see the expressions of the Nukiyama–Tanasawa distribution in Tables 1 and 2), than those of other modeling PDFs.

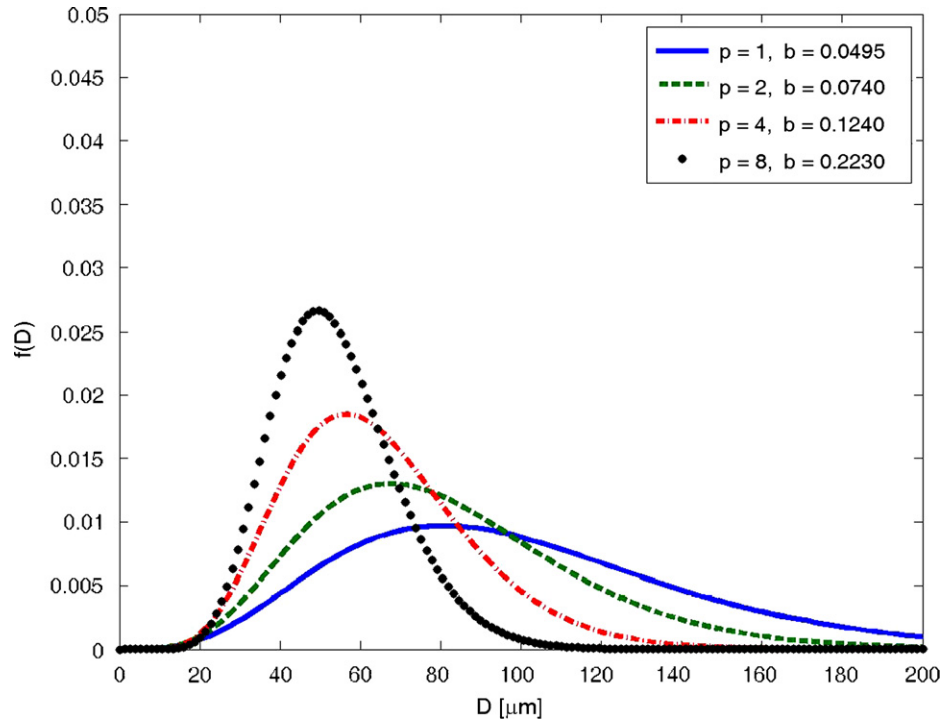


Fig. 9. Analytical PDFs of the Nukayama–Tanasawa distribution for the various widths.

Table 7  
Input parameters for the initial conditions using Nukiyama–Tanasawa PDF

Case	$p$	$b$
13	1	0.0495
14	2	0.0740
15	4	0.1240
16	8	0.2230

Note that  $c$  is set as a unity.

## 5. Conclusions

Because of the difficulty of optical access in the nozzle exit region, which makes initial distribution of a turbulent water spray impossible to obtain, initial distribution was modeled with well-known PDFs such as Rosin–Rammler, log-normal, Gaussian, and Nukiyama–Tanasawa. The distribution width of each PDF was varied for each spray simulation. Since the representative diameter at the nozzle exit was needed to be known for an input of the modeled PDFs, the arithmetic mean diameter at the nozzle exit was extrapolated using the second order least-square fit with the experimental data of the downstream locations. For statistically reliable data, droplet characteristics of the computation were obtained at quasi-steady state. Computational results were then compared with the experimental data. Overall, it was found that all PDF models were

satisfactorily applicable when modeled PDFs were confirmed able to reproduce droplet characteristics which data are within 20% of the experimental data. However, it is cautioned that the varying parameters (i.e.,  $q$  for the Rosin–Rammler,  $\sigma_{ln}^*$  for the log-normal,  $\sigma$  for the Gaussian,  $p$  and  $b$  for the Nukiyama–Tanasawa PDFs), must be optimized to yield realistic modeling. Among the tested distributions, the Nukiyama–Tanasawa PDF best described the initial condition because of the amount of freedom in controlling adjustable parameters. It is noteworthy to re-iterate that all types of the PDFs may well be suitable as an initial condition with an appropriate value for the PDFs' specific constants. However, it is cautioned that the process of finding the right constants for the PDFs may require numerous trial-and-error computations, even if an arithmetic average diameter at the nozzle exit were known. It is also cautioned that obtaining the arithmetic mean diameter at the nozzle exit is not an easy task. One can only predict the exit mean diameter by performing a direct liquid-core computation, as in Refs. [4,5] or one needs to extrapolate a mean value using experimental data, as in this current report.

As for the physical aspect of the spray, a gradation of particle sizes in the radial direction occurred due to different dynamic behavior of small and large particles. Large particles were dispersed by the spray initial cone angle and subsequent interactions with turbulent eddies in the entrained air, while smaller particles were generally swept toward the spray centerline by aerodynamic drag interactions with the entrained air.

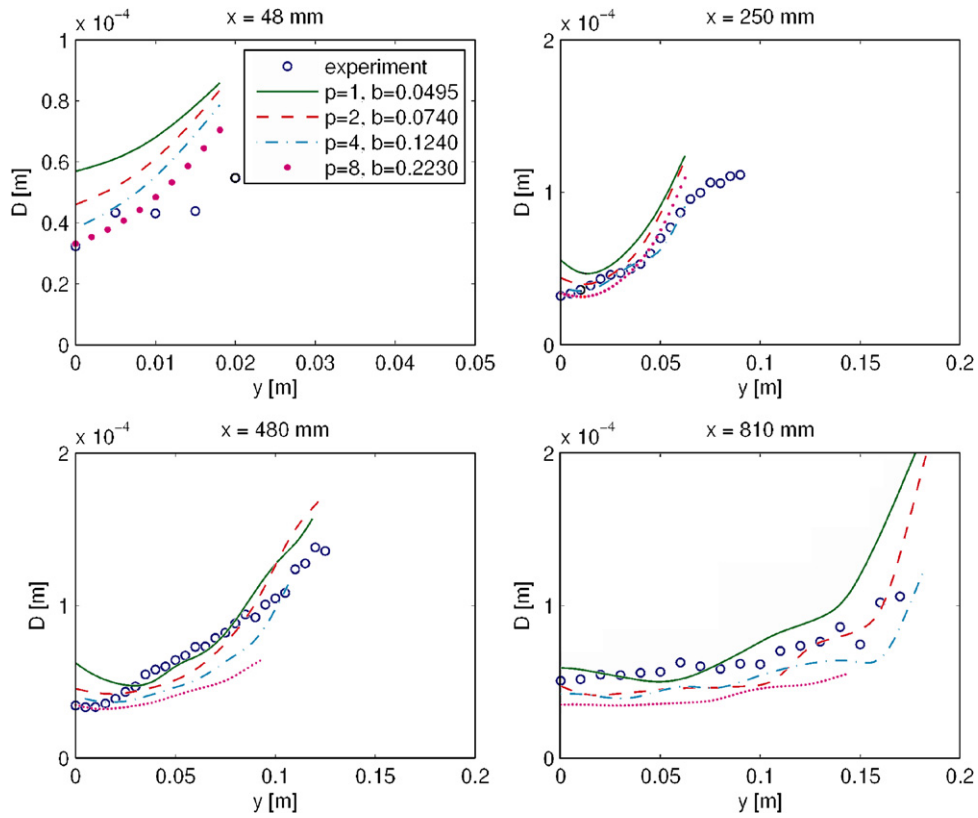


Fig. 10. Mean droplet size variation at different axial locations. The Nukiyama–Tanasawa distribution is used for the initial droplet size.

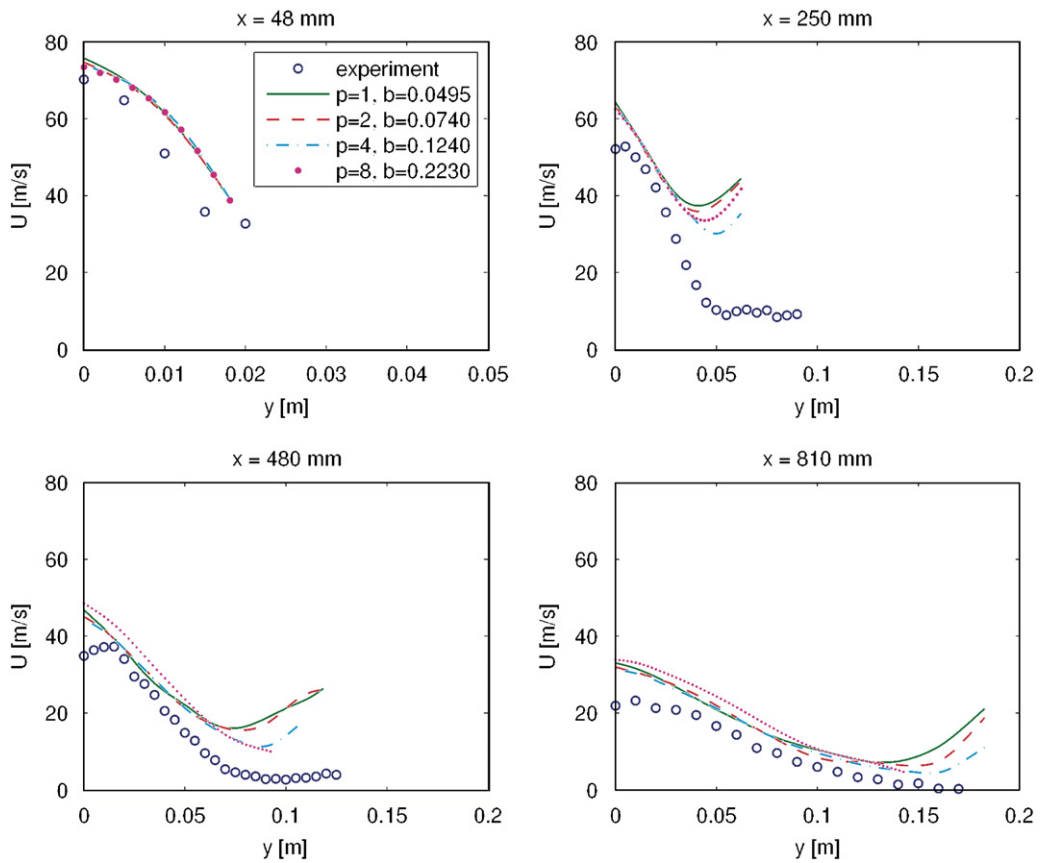


Fig. 11. Mean droplet speed variation at different axial locations. The Nukiyama–Tanasawa distribution is used for the initial droplet size.

## Acknowledgments

The first author acknowledges that this research was conducted during his stay at Sandia National Laboratories. Sandia is a multi-program laboratory operated by Sandia Corporation, a Lockheed Martin Company, for the United States Department of Energy's National Nuclear Security Administration under contract DE-AC04-94AL85000. The authors are grateful for the useful discussion shared by Dr. Sheldon Tieszen and Prof. Paul DesJardin of University of Buffalo. Our sincere thanks go to Dr. Reed Skaggs of US Army Research Laboratory for providing the experimental image of Fig. 2. The first author wishes to acknowledge the partial support of this research by a Grant R0504532 from Carbon Dioxide Reduction and Sequestration Research Center of Korea and the New Faculty Research Grant, funded by the Korea University.

## References

- [1] Skaggs R, Canami A. Hydrodynamic ram experiments for the validation of the fire prediction model. ARL-TR-3238, July 2004.
- [2] Yoon SS, Jepsen RA, Nissen MR, O'Hern TJ. Experimental investigation on splashing and nonlinear fingerlike instability of large water drops. *J Fluids Struct* 2007;23:101–15.
- [3] MacPhee AG, Tate MW, Powell CF, Yue Y, Renzi MJ, Ercan A, et al. X-ray imaging of shock waves generated by high-pressure fuel sprays. *Science* 2002;295:1261.
- [4] Yoon SS. Droplet distributions at the liquid core of a turbulent spray. *Phys Fluids* 2005;17:035103.
- [5] Park H, Yoon SS, Heister SD. A nonlinear atomization model for computation of drop-size distributions and complete spray simulation. *Int J Numer Methods Fluids* 2005;48:1219–40.
- [6] Babinsky E, Sojka PE. Modeling drop size distributions. *Progr Energy Combustion Sci* 2002;28:303–29.
- [7] Hwang SS, Liu Z, Reitz RD. Breakup mechanisms and drag coefficients of high-speed vaporizing liquid drops. *Atomization and Sprays* 1996;6:353–76.
- [8] DesJardin PE, Gritzo LA. A dilute spray model for fire simulations: formulation, usage and benchmark problems. Sandia National Laboratories Technical Report, No. SAND2002-3419, Albuquerque; 2002.
- [9] Amsden AA, Ramshaw JD, O'Rourke PJ, Dukowicz JK. KIVA: A computer program for two and three dimensional fluid flows with chemical reactions and fuel sprays. LA-10245-MS, UC-32 and UC-34; 1985.
- [10] O'Rourke PJ. Collective drop effects on vaporizing liquid sprays. PhD thesis, Princeton University; 1981.
- [11] Hewson JC, Yoon SS. On sampling from prescribed droplet pdfs using computational parcels. *Atomization and Sprays* 2005;15:119–31.
- [12] Crowe C, Sommerfeld M, Tsuji Y. Multiphase flows with droplets and particles. Boca Raton, FL: CRC Press; 1998.
- [13] Jones WP, Launder BE. The prediction of laminarization with a two-equation model of turbulence. *Int J Heat Mass Transfer* 1972;15:301–14.
- [14] Patankar SV. Numerical heat transfer and fluid flow. New York: Taylor & Francis; 1980.
- [15] Faeth GM. Evaporation and combustion in sprays. *Progr Energy Combustion Sci* 1983;9:1–76.
- [16] Faeth GM. Mixing, transport and combustion in sprays. *Progr Energy Combustion Sci* 1987;13:293–345.
- [17] Sallam KA, Faeth GM. Drop formation at the surface of plane turbulent liquid jets in still gases. *Int J Multiphase Flow* 1999;28:427–49.
- [18] Sallam KA, Faeth GM. Liquid breakup at the surface of turbulent round liquid jets in still gases. *Int J Multiphase Flow* 2002;29:167–70.
- [19] Ranz WE, Marshall WR. Evaporation from drops: part I. *Chem Eng Progress* 1952;48:141–6.
- [20] Ranz WE, Marshall WR. Evaporation from drops: part II. *Chem Eng Progress* 1952;48:173–80.
- [21] Maxey MR, Riley JJ. Equation of motion for a small rigid sphere in a non-uniform flow. *Phys Fluids* 1983;26:883–9.
- [22] Ko GH, Lee SH, Ryou HS, Choi YK. Development and assessment of a hybrid droplet collision model for two impinging sprays. *Atomization and Sprays* 2003;13:251–72.
- [23] Georjon TL, Reitz RD. A drop-shattering collision model for multidimensional spray computations. *Atomization and Sprays* 1999;9:231–54.
- [24] O'Rourke PJ, Amsden AA. The TAB method for numerical calculation of spray droplet breakup. SAE Technical Paper, 872089; 1987.
- [25] Gosman AD, Ioannides E. Aspects of computer simulation of liquid-fueled combustion. AIAA Paper, AIAA-81-0323; 1981.
- [26] Shuen JS, Chen LD, Faeth GM. Evaluation of a stochastic model of particle dispersion in a turbulent round jet. *AIChE J* 1983;29:167–70.
- [27] Zhou A, Yao SC. Group modeling of impacting spray dynamics. *Int J Heat Mass Transfer* 1992;35(1):121–9.
- [28] Didonato AR, Morris Jr AH. Computation of the incomplete gamma function ratios and their inverse. *ACM Trans Math Software* 1986;12(4):377–93.
- [29] Wu KJ, Reitz RD, Bracco FV. Measurements of drop size at the spray edge near the nozzle in atomizing liquid jets. *Phys Fluids* 1986;29:941–51.
- [30] Taylor BN, Kuyatt CE. Guidelines for evaluating and expressing the uncertainty of NIST measurement results. NIST Technical Note 1297, National Institute of Standards and Technology, Gaithersburg, MD; 1994.